Int. J. Solids Structures Vol. 24, No. 1, pp. 77–87, 1988
Printed in Great Britain.

0020-7683/88 $3.00 + .00

PENETRATION OF REINFORCED CONCRETE WITH OGIVE-NOSE PENETRATORS†

M. J. Forrestal, V. K. Luk and H. A. Watts
Sandia National Laboratories, Albuquerque, NM 87185, U.S.A.

(*Received* 11 *February* 1987; *in revised form* 22 *July* 1987)

Abstract—We developed a model to estimate forces on ogive-nose penetrators launched into reinforced-concrete targets. Post-test target observations and triaxial tests on samples cored from concrete slabs guided the model development. The cylindrical, cavity-expansion approximation simplified the analysis to one-dimensional, radial motion, and an iterative procedure provided the solution technique for the partial differential equations. Graphical results show forces on nose shapes for a practical range of penetration velocities.

INTRODUCTION

Studies on penetration of non-deforming projectiles into concrete and geological targets usually focus on the prediction and measurement of penetration depth or deceleration history[1]. Theoretical models use solution techniques that may be grouped into three main categories: empirical equations fit to test data[2]; models that approximate the target response by one-dimensional motion using cavity-expansion methods[3]; and wave-code analyses[4].

For this study, we used the cylindrical, cavity-expansion approximation. As shown in Fig. 1, this approximation idealized the target as thin, independent layers normal to the penetration direction and simplified the analyses to one-dimensional motion in the radial direction. Triaxial material tests[5] on samples cored from concrete targets used for full-scale, penetration tests guided the choice of constitutive models. Figure 2 shows pressure–volumetric strain and shear strength – pressure data for concrete samples that were tested at 4, 24, and 48 months. We approximated these data with a linear, pressure–volumetric strain relation and a constant, shear strength (Tresca) failure criterion.

Post-test, reinforced-concrete targets have a conical shaped entry crater followed by a tunnel with nearly the same penetrator diameter. Crater depths are usually one to two nose lengths depending on the location of the reinforcing rods from the free surface of the targets. Although we have no available penetrator, deceleration-time data for reinforced-concrete targets, deceleration-time profiles for rock targets[1] show a monotonic rise to a peak value at about the time the tunnel is developed. The cylindrical, cavity-expansion assumption approximates this tunnel phase of penetration. In addition, we assumed that the only function of the reinforcement was to prevent radial cracks from circumferential tensile stresses.

Earlier penetration models[6–8] used the locking-solid approximation to represent pressure–volumetric strain data. However, Fig. 2 shows that this relationship is nearly linear for pressures to about 400 MPa. If, however, pressure–volumetric strain data for different target materials indicate that the locking-solid approximation may be adequate, closed-form equations that estimate forces on cone-nose and ogive-nose penetrators are available. More recently, Forrestal[1] derived closed-form equations for the motion of cone-nose penetrators into targets described with linear, pressure–volumetric strain relations. Within the framework of the cylindrical, cavity-expansion approximation, cone-nose penetrators produce constant, cavity-expansion velocities and permit the use of a similarity transformation. This transformation reduces the partial differential equations that govern radial motion to ordinary differential equations. The resulting differential equations are solved numerically[9] or in closed form with an iterative technique[1].

---

† This work was supported by the U.S. Department of Energy.

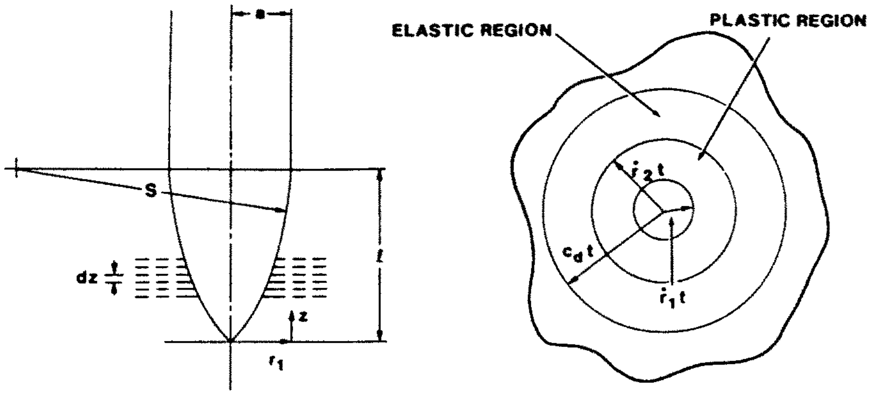

Fig. 1. Geometry of ogival nose and target response regions.

Ogive-nose penetrators (see Fig. 1) do not produce a uniform cavity expansion. Therefore, the governing equations cannot be reduced to ordinary differential equations with a similarity transformation. Thus, for this study, we solved the partial differential equations with an iterative technique. In the following sections we derive expressions for forces on ogive-nose penetrators as a function of penetration velocity and present parametric results for several ogive-nose shapes.

PROBLEM FORMULATION

A rigid projectile with an ogival nose penetrates a uniform target at normal incidence. As shown in Fig. 1, the problem is axisymmetric and simplified further by using the cylindrical, cavity-expansion approximation. The ogival nose traveling at penetration velocity V opens a circular cavity in a target layer at time $t = 0$. Figure 1 shows that an ogive is the arc of a circle with radius s and is tangent to the cylindrical aft-body. The nose shape specifies the cavity radius r_1 and the cavity-expansion velocity $\mathrm{d}r_1/\mathrm{d}t$. Thus

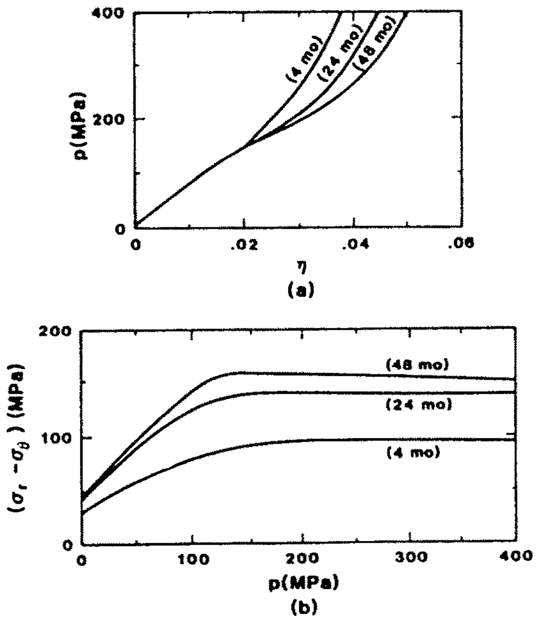

Fig. 2. Triaxial data[5]: (a) pressure–volumetric strain; (b) shear strength–pressure.

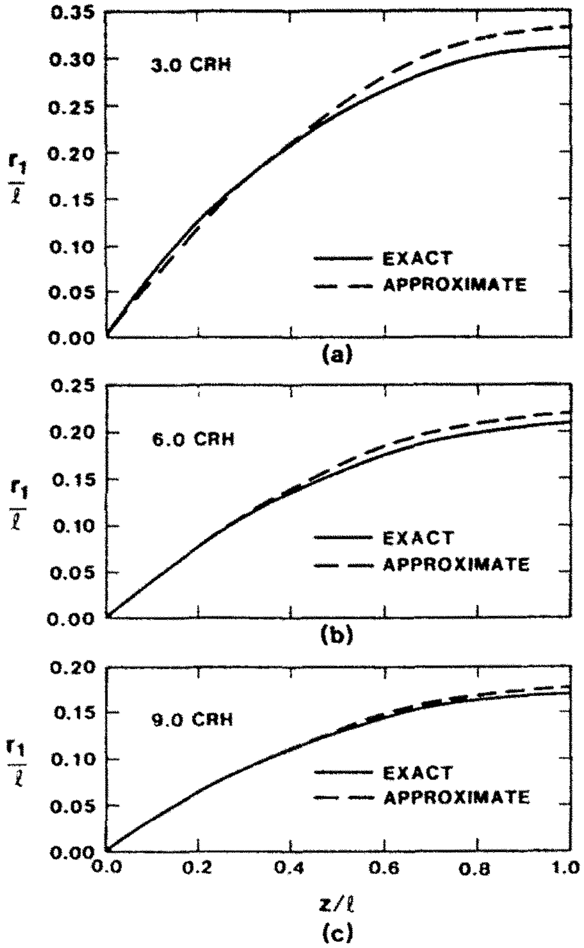

Fig. 3. Polynomial approximations to ogival geometry.

$$r_1 = [s^2 - (l - z)^2]^{1/2} - (s - a), \quad z = Vt \tag{1a}$$

$$\frac{dr_1}{dt} = \frac{V(l - Vt)}{s}\left[1 - \left(\frac{l - Vt}{s}\right)^2\right]^{-1/2} \tag{1b}$$

where l is the nose length and a the aft-body radius. It is common to define an ogival nose in terms of caliber radius head

$$CRH = s/2a. \tag{1c}$$

Next, we approximate the ogival nose and cavity-expansion velocity with the polynomial approximations

$$r_1 = \alpha t\left(1 - \frac{1}{2}\frac{Vt}{l}\right) \tag{2a}$$

$$\frac{dr_1}{dt} = \alpha(1 - Vt/l) \tag{2b}$$

$$\alpha = \frac{Vl}{s - a}. \tag{2c}$$

The constant α depends on the nose shape (CRH) and is obtained from the initial condition that the cavity starts with zero radius. An additional criterion requires that the cavity-expansion velocity vanishes at a nose length of penetration. Figures 3(a)–(c) show that this polynomial expression is accurate.

As shown in Fig. 1, cylindrical cavity-expansion produces two annular response regions—a plastic region next to the cavity wall and an elastic region. The plastic region is described by linear fits to the triaxial test data (Fig. 2). Pressure–volumetric strain and the Tresca yield criterion are

$$p = K(1-\rho_0/\rho) = K\eta \tag{3a}$$

$$\sigma_r - \sigma_\theta = Y \tag{3b}$$

where p is the hydrostatic pressure; ρ_0, ρ are densities in the undeformed and deformed configurations; η is the volumetric strain; σ_r, σ_θ are radial and circumferential stress components (positive in compression); and Y is the flow stress. The elastic region has bulk modulus K and Poisson's ratio ν.

The plastic region (Fig. 1) is bounded by the radii, $r_1(t)$ and $r_2(t)$; where r is the radial Eulerian coordinate; t is time; and $\mathrm{d}r_2(t)/\mathrm{d}t$ is the propagation velocity of the elastic–plastic interface. Equations of mass and momentum conservation in cylindrical Eulerian coordinates are

$$\frac{\partial\rho}{\partial t} + \frac{1}{r}\frac{\partial}{\partial r}(r\rho v) = 0 \tag{4a}$$

$$\frac{\partial\sigma_r}{\partial r} + \frac{\sigma_r - \sigma_\theta}{r} = -\rho\left(\frac{\partial v}{\partial t} + v\frac{\partial v}{\partial r}\right) \tag{4b}$$

where v is the radial particle velocity (positive outward). As suggested by Hill[10], the axial stress is taken as $\sigma_z = (\sigma_r + \sigma_\theta)/2$. Thus, pressure becomes $p = (\sigma_r + \sigma_\theta)/2$. Next, the nonlinear equations for the plastic region are combined to eliminate σ_θ, ρ. The resulting two equations in σ_r and v are

$$\frac{\partial v}{\partial r} + \frac{v}{r} = \frac{-1}{K(1-\eta)}\left(\frac{\partial\sigma_r}{\partial t} + v\frac{\partial\sigma_r}{\partial r}\right) \tag{5a}$$

$$\frac{\partial\sigma_r}{\partial r} + \frac{Y}{r} = \frac{-\rho_0}{(1-\eta)}\left(\frac{\partial v}{\partial t} + v\frac{\partial v}{\partial r}\right). \tag{5b}$$

Post-analyses evaluation and the data in Fig. 2(a) showed η small compared with unity, and $(1-\eta)$ is replaced with unity in eqns (5a) and (5b).

The elastic region (Fig. 1) is bounded by the radii $r_2(t)$ and $c_d t$ where c_d is the elastic, dilatational, wave velocity. We are primarily concerned with calculating radial stress in the plastic region at the cavity wall in order to obtain penetration resistance. To calculate penetration resistance, only radial stress and particle velocity in the elastic region at the elastic–plastic interface are required. In addition, we approximate the elastic-interface radial stress and particle velocity with the functional forms derived for quasi-static solutions[1, 10]. We show, later, no loss in accuracy with this approximation. Thus, the elastic radial stress at $r = r_2$ is taken as

$$\sigma_e = \frac{Y}{2}\left\{1 + \frac{\psi^2}{(1-2\nu)(1-\psi^2)^{1/2}}\ln\left[\frac{1+(1-\psi^2)^{1/2}}{\psi}\right]\right\} \tag{6a}$$

where

$$\psi = \frac{1}{c_d}\frac{\mathrm{d}r_2}{\mathrm{d}t}, \quad c_d^2 = c_p^2\left[\frac{3(1-\nu)}{(1+\nu)}\right], \quad c_p^2 = \frac{K}{\rho_0} \tag{6b}$$

and the elastic particle velocity at $r = r_2$ is

$$v_e = \frac{(1+\nu)}{3(1-2\nu)}\left(\frac{Y}{K}\right)\frac{dr_2}{dt}. \tag{6c}$$

The elastic and plastic regions are linked with the Hugoniot jump conditions that conserve mass and momentum across the wave-front. These mass and momentum conditions are

$$\rho_p\left(v_p - \frac{dr_2}{dt}\right) = \rho_0\left(v_e - \frac{dr_2}{dt}\right) \tag{7a}$$

$$\sigma_p + \rho_p v_p\left(v_p - \frac{dr_2}{dt}\right) = \sigma_e + \rho_0 v_e\left(v_e - \frac{dr_2}{dt}\right) \tag{7b}$$

where σ_p and v_p are the plastic-interface radial stress and particle velocity, respectively. In eqns (7a) and (7b), $\rho_e = \rho_0$ because $p = 0$ in the elastic region[10].

Net axial force is derived in Ref. [8] and given by

$$F_z = 2\pi\int_0^{\chi} \sigma_r(r_1)r_1\frac{dr_1}{dz}dz \tag{8}$$

where r_1 is given by eqn (1a) and $z = \chi$ corresponds to the axial position where the target separates from the ogival nose.

SOLUTION PROCEDURE

For convenience, we introduce the dimensionless variables

$$S = \frac{\sigma_r}{K};\quad T = \frac{Y}{K} \tag{9a}$$

$$\xi = \frac{r}{l};\quad \dot{\xi} = \frac{1}{V}\frac{dr}{dt};\quad \tau = \frac{Vt}{l} \tag{9b}$$

$$U = \frac{v}{V};\quad \lambda_p = \frac{V}{c_p};\quad \lambda_d = \frac{V}{c_d} \tag{9c}$$

where a dot refers to differentiation with respect to τ.

Boundary conditions at the cavity wall and field equations for the plastic region transform to

$$\xi_1(\tau) = \alpha_0\tau(1-\tau/2) \tag{10a}$$

$$\dot{\xi}_1(\tau) = \alpha_0(1-\tau) \tag{10b}$$

$$\alpha_0 = \frac{l}{s-a} \tag{10c}$$

and

$$\frac{\partial U}{\partial \xi} + \frac{U}{\xi} = -\left(\frac{\partial S}{\partial \tau} + U\frac{\partial S}{\partial \xi}\right) \tag{11a}$$

$$\frac{\partial S}{\partial \xi} + \frac{T}{\xi} = -\lambda_p^2\left(\frac{\partial U}{\partial \tau} + U\frac{\partial U}{\partial \xi}\right). \tag{11b}$$

Boundary conditions for the plastic region at the elastic–plastic interface are obtained from eqns (6) and (7). The dimensionless radial stress and particle velocity in the plastic region at the elastic–plastic interface ($\xi = \xi_2$) are

$$S_p = \frac{T}{2}\left\{1+\frac{\psi^2}{(1-2\nu)(1-\psi^2)^{1/2}(1-\xi_2^2\lambda_p^2\omega^2)}\ln\left[\frac{1+(1-\psi^2)^{1/2}}{\psi}\right]\right\} \tag{12a}$$

$$U_p = \frac{\xi_2 T}{(1-2\nu)}\left\{\frac{(1+\nu)}{3}-\frac{\omega\psi^2}{2(1-\psi^2)^{1/2}(1-\xi_2^2\lambda_p^2\omega^2)}\ln\left[\frac{1+(1-\psi^2)^{1/2}}{\psi}\right]\right\} \tag{12b}$$

in which

$$\omega = \frac{(1+\nu)T}{3(1-2\nu)}-1, \quad \psi = \xi_2\lambda_d. \tag{12c}$$

Solutions to the non-linear, partial differential equations, eqns (11a) and (11b), are obtained with an iterative procedure. First, set the right-hand side of eqn (11a) to zero and solve for U

$$U^0(\xi,\tau) = f(\tau)\xi^{-1}. \tag{13a}$$

The function $f(\tau)$ is evaluated from the boundary condition at the cavity wall $U^0(\xi = \xi_1, \tau) = \dot{\xi}_1$. From eqns (10b) and (10c)

$$U^0(\xi,\tau) = A\xi^{-1} \tag{13b}$$

$$A = \alpha_0^2\tau(1-\tfrac{3}{2}\tau+\tfrac{1}{2}\tau^2). \tag{13c}$$

Next, substitute eqn (13b) into the right-hand side of eqn (11b) and integrate. This first approximation to radial stress is

$$S^0(\xi,\tau) = S_p+(T+\lambda_p^2B)\ln\left(\frac{\xi_2}{\xi}\right)+\tfrac{1}{2}\lambda_p^2A^2\left(\frac{1}{\xi_2^2}-\frac{1}{\xi^2}\right) \tag{14a}$$

$$B = \alpha_0^2(1-3\tau+\tfrac{3}{2}\tau^2). \tag{14b}$$

As with eqn (13a), integration of eqn (11b) yields a function $g(\tau)$ that is evaluated with eqn (12a).

This procedure is repeated to obtain the second approximations to particle velocity U^1 and radial stress S^1. The integration functions $f(\tau)$, $g(\tau)$ are evaluated with the jump conditions, eqns (12a) and (12b). Thus

$$U^1(\xi,\tau) = \xi M_1+\frac{M_2}{\xi}+\frac{M_3}{\xi^3}+\ln\left(\frac{\xi_2}{\xi}\right)\left(\xi M_4+\frac{M_5}{\xi}\right) \tag{15}$$

$$\begin{aligned}S^1(\xi,\tau) = S_p+\frac{\lambda_p^2}{2}&\left\{(\xi_2^2-\xi^2)\left(N_1+\frac{N_4}{2}+M_1^2\right)+\left(\frac{1}{\xi_2^2}-\frac{1}{\xi^2}\right)(M_2^2+2M_1M_3-N_3)\right.\\&+2\left(\frac{1}{\xi_2^4}-\frac{1}{\xi^4}\right)M_2M_3+\left(\frac{1}{\xi_2^6}-\frac{1}{\xi^6}\right)M_3^2+2\ln\left(\frac{\xi_2}{\xi}\right)\left[\frac{T}{\lambda_p^2}+N_2-\tfrac{1}{2}\xi^2N_4\right.\\&\left.\left.-\left(\xi M_1+\frac{M_2}{\xi}+\frac{M_3}{\xi^3}\right)\left(\xi M_4+\frac{M_5}{\xi}\right)\right]+\left[\ln\left(\frac{\xi_2}{\xi}\right)\right]^2\left[N_5-\left(\xi M_4+\frac{M_5}{\xi}\right)^2\right]\right\}\end{aligned} \tag{16}$$

in which M_i and N_i are functions of τ

$$M_1 = -\frac{1}{2}\left[\dot{S}_p - \tfrac{3}{2}(\lambda_p\alpha_0)^2(1-\tau) + \frac{\dot{\xi}_2(T+\lambda_p^2B)}{\xi_2} + \frac{\lambda_p^2AB}{\xi_2^2} - \frac{\dot{\xi}_2\lambda_p^2A^2}{\xi_2^3}\right] \tag{17a}$$

$$M_2 = \frac{1}{2}\left\{\xi_2[2U_p + \xi_2\dot{S}_p + \dot{\xi}_2(T+\lambda_p^2B) - \tfrac{3}{2}\xi_2(\lambda_p\alpha_0)^2(1-\tau)] + \lambda_p^2A\left(B - \frac{\dot{\xi}_2A}{\xi_2} - \frac{A^2}{\xi_2^2}\right)\right\} \tag{17b}$$

$$M_3 = \tfrac{1}{2}\lambda_p^2A^3 \tag{17c}$$

$$M_4 = \tfrac{3}{2}(\lambda_p\alpha_0)^2(1-\tau) \tag{17d}$$

$$M_5 = -A(T+2\lambda_p^2B) \tag{17e}$$

and

$$N_1 = \frac{1}{2}\left\{-\ddot{S}_p - \tfrac{3}{2}(\lambda_p\alpha_0)^2 - \frac{1}{\xi_2}[\ddot{\xi}_2(T+\lambda_p^2B) - 6\dot{\xi}_2(\lambda_p\alpha_0)^2(1-\tau)]\right.$$
$$+ \frac{1}{\xi_2^2}[\dot{\xi}_2^2(T+\lambda_p^2B) - \lambda_p^2B^2 + 3(\lambda_p\alpha_0)^2A(1-\tau)]$$
$$\left. + \frac{\lambda_p^2A(4\dot{\xi}_2B + \ddot{\xi}_2A)}{\xi_2^3} - \frac{3\dot{\xi}_2^2A^2}{\xi_2^4}\right\} \tag{18a}$$

$$N_2 = \dot{\xi}_2U_p + \xi_2\dot{U}_p + \frac{\xi_2^2}{4}[2\ddot{S}_p + 3(\lambda_p\alpha_0)^2] + \tfrac{1}{2}(\xi_2\ddot{\xi}_2 + \dot{\xi}_2^2)(T+\lambda_p^2B)$$
$$+ \xi_2\dot{\xi}_2[\dot{S}_p - 3(\lambda_p\alpha_0)^2(1-\tau)] + \tfrac{1}{2}\lambda_p^2[B^2 - 3\alpha_0^2A(1-\tau)]$$
$$- \frac{A}{2\xi_2}\left[2\dot{\xi}_2(T+3\lambda_p^2B) + \lambda_p^2A\left(\ddot{\xi}_2 - \frac{\dot{\xi}_2^2-3B}{\xi_2} - \frac{2\dot{\xi}_2A}{\xi_2^2}\right)\right] \tag{18b}$$

$$N_3 = \tfrac{3}{2}\lambda_p^2A^2B \tag{18c}$$

$$N_4 = -\tfrac{3}{2}(\lambda_p\alpha_0)^2 \tag{18d}$$

$$N_5 = -\{2\lambda_p^2[B^2 - 3\alpha_0^2A(1-\tau)] + TB\}. \tag{18e}$$

As discussed by Hunter[11], the elastic–plastic interface velocity $\dot{\xi}_2$ depends on the cavity-expansion velocity $\dot{\xi}_1$. This interface velocity is calculated from the boundary condition at the cavity wall

$$U^1(\xi = \xi_1, \tau) = \dot{\xi}_1 \tag{19}$$

where $\dot{\xi}_1$ is given by eqn (10b).

After rearrangement, eqns (10b) and (19) are written as an explicit, ordinary differential equation in ξ_2

$$\ddot{\xi}_2 = \frac{1}{DEN}\left\{\frac{A - \xi_2U_p}{[\xi_2^2 - (\tau\alpha_0)^2(1-\frac{1}{2}\tau)^2]} + \tfrac{3}{4}(\lambda_p\alpha_0)^2(1-\tau) - \frac{\dot{\xi}_2(T+\lambda_p^2B)}{2\xi_2}\right.$$
$$- \frac{(\lambda_p\alpha_0)^2A(2-5\tau+\frac{5}{2}\tau^2)}{2\xi_2^2} + \frac{\dot{\xi}_2\lambda_p^2A^2}{2\xi_2^3}$$
$$\left. + \frac{A[T + (\lambda_p\alpha_0)^2(2 - \frac{15}{2}\tau + \frac{15}{4}\tau^2)]}{[\xi_2^2 - (\tau\alpha_0)^2(1-\frac{1}{2}\tau)^2]}\ln\left[\frac{\xi_2}{\tau\alpha_0(1-\frac{1}{2}\tau)}\right]\right\} \tag{20a}$$

$$DEN = \frac{T\psi\lambda_{\mathrm{d}}}{4(1-2\nu)(1-\psi^2)[1-(\dot{\xi}_2\lambda_{\mathrm{p}}\omega)^2]}\left\{\frac{2-\psi^2[1+(\dot{\xi}_2\lambda_{\mathrm{p}}\omega)^2]}{(1-\psi^2)^{1/2}[1-(\dot{\xi}_2\lambda_{\mathrm{p}}\omega)^2]} \times \ln\left[\frac{1+(1-\psi^2)^{1/2}}{\psi}\right]-1\right\}. \quad (20b)$$

The numerical solution procedure for this ordinary differential equation is described in the next section. Solutions of ξ_2, $\dot{\xi}_2$, and $\ddot{\xi}_2$ are used to evaluate the radial stress on the ogival nose S^1 $(\xi = \xi_1, \tau)$ in eqn (16). When S^1 $(\xi = \xi_1, \tau)$ becomes zero, the ogival nose loses contact with the target.

As discussed by Hunter[11], we must also show that work performed in the plastic region is everywhere non-negative. From the procedure outlined by Hunter[11], this condition is given by

$$\frac{U}{\xi} - \frac{\partial U}{\partial \xi} \geqslant 0 \quad \text{for} \quad \xi_1 < \xi < \xi_2. \quad (21)$$

We show later that this criterion is satisfied for the applications of this study.

In terms of the dimensionless variables, the net axial force on the ogival nose, eqn (8), is

$$F_z = 2\pi a^2 K(4CRH-1)\int_0^{\varepsilon} S^1(\xi_1, \tau)\xi_1\dot{\xi}_1 \, \mathrm{d}\tau \quad (22)$$

where CRH is given by eqn (1c) and ε is the dimensionless time at separation.

Projectile velocity V and cavity-expansion velocity decrease with penetration depth. At the end of the trajectory, data[1] from instrumented tests show deceleration jumps from a finite value to zero. Thus, for arbitrarily small velocity V, there is a finite, quasi-static force on the penetrator nose. Quasi-static, radial stress from a cylindrical, cavity-expansion analysis[1] is

$$S_s = \frac{T}{2}\left\{1+\ln\left[\frac{6(1-2\nu)}{(5-4\nu)T}\right]\right\} \quad (23a)$$

and the quasi-static, axial force is

$$F_{zs} = \pi a^2 K S_s. \quad (23b)$$

This closed-form expression F_{zs} provides a check for the numerical evaluation of eqn (22) for V approaching zero.

NUMERICAL EVALUATION

For this study, we focus on the radial stress distribution on the nose and axial force. $S^1(\xi, \tau)$ and F_z depend on the elastic-plastic, wave-front location ξ_2, where ξ_2 is in the form of a non-linear, differential equation. Because $\ddot{\xi}_2$ is singular at $\tau = 0$, the solution in the neighborhood of the nose tip ($\tau \leqslant \tau_0 = 0.001$) is computed by neglecting the second term in eqn (2a) that reduces the solution to that of a conical nose given in Ref. [1]. An outline for the computation for $\tau \geqslant 0.001$ is:

(i) solve the differential equation for ξ_2 given by eqns (20),

(ii) numerically evaluate $\dddot{\xi}_2$ that is involved to compute S^1 $(\xi = \xi_1, \tau)$ in eqn (16) (the involvement of $\dddot{\xi}_2$ arises from $\dot{S}_{\mathrm{p}}$, see eqn (12a), and N_1 and N_2, eqns (18a) and (18b),

(iii) compute S^1 $(\xi = \xi_1, \tau)$ and continually monitor to ensure the values are positive; as previously mentioned, the target separates from the nose when radial stress becomes tensile, and

(iv) compute axial force in eqn (22).

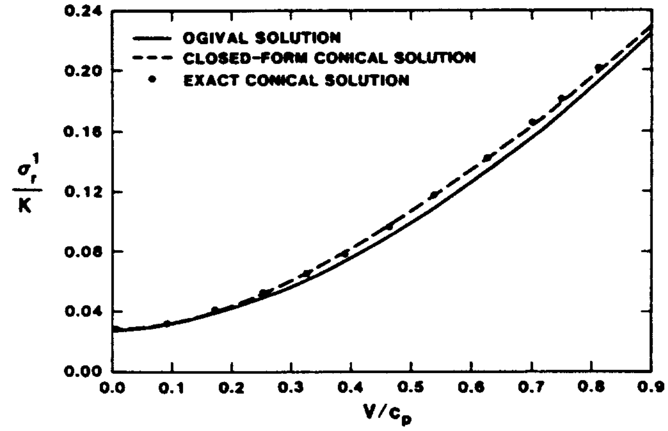

Fig. 4. Comparison of radial stress at $z/l = 0.01$ for a 6.0-*CRH* ogival nose and a conical nose that neglects the second term in eqn (2a) penetrating reinforced concrete with $Y = 95$ MPa.

The ODE code RDEAM[11] can solve the differential equation in eqns (20) while searching for a root of the S^1 function. However, a complication arises in that $\dddot{\xi}_2$ is needed. We decided to obtain this quantity through a numerical procedure rather than by the complicated, analytical process of differentiating the differential equation, eqns (20). A natural approach is to use the underlying polynomial interpolants in the Adams integration methods used by RDEAM. This necessitated a modification of the output interpolation process to provide an approximation to the next higher order derivative. Since the integrand function for the axial force in eqn (22) depends on the initial-value problem solution and its derivatives, it is most convenient to perform the quadrature of the force integral as an initial-value differential equation. However, because this force integral also depends on $\dddot{\xi}_2$, which is approximated by the output interpolation process in the modified RDEAM, this equation cannot be carried along simultaneously with the differential equations for ξ_2. Rather, another integration code must be utilized for this separate task. A one-step method is the most appropriate in these circumstances; the Runge–Kutta code DERKF[13] was utilized.

In summary, following a successful step by the root-solving ODE code (which then defines the interpolant used in approximating ξ_2, $\dot{\xi}_2$, $\ddot{\xi}_2$, and $\dddot{\xi}_2$ over that step), the Runge–Kutta method advances the force integral computation over the very same step. This procedure is continued until the root ε of $S^1(\tau) = 0$ is encountered. At this time, the desired force integral evaluation is completed.

NUMERICAL RESULTS AND DISCUSSION

In this section, we present numerical results for rigid, ogive-nose penetrators and a concrete target. Figure 2 presents pressure-volumetric strain and shear strength-pressure data, and eqns (3a) and (3b) model these data. The 4-month concrete is described by $\rho_0 = 2.20 \times 10^3$ kg m^{-3}, $K = 9.0$ GPa, $Y = 95$ MPa, $\nu = 0.27$, and $c_p = 2020$ m s^{-1}.

Figure 4 shows radial stress vs penetration velocity from three calculations near the tip ($z/l = 0.01$; Fig. 1) of a 6.0-*CRH* nose. The conical nose results[1] neglect the second term in eqn (2a) and are the exact solution from numerical evaluation of a non-linear differential equation and a closed-form, iterative solution. Figure 4 shows excellent agreement between the conical solutions and very close agreement between the conical and ogival solutions. This close agreement is a check on the numerical procedure described in the last section and offers justification for approximations (6a) and (6c) used for the elastic stress and particle velocity at the elastic–plastic wave-front. We attribute the small difference between the conical solution and the ogival solution with $z = 0.01$ to the elastic, wave-front approximations. In addition, close agreement with the exact, conical solution justifies the iterative procedure used to obtain the ogival solution.

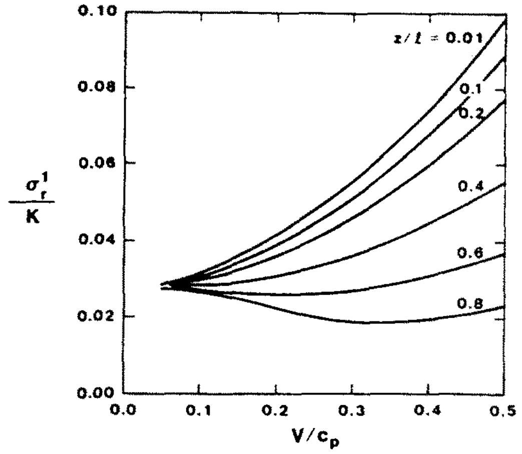

Fig. 5. Radial stress on 6.0-*CRH* ogival nose vs penetration velocity for reinforced concrete with $Y = 95$ MPa.

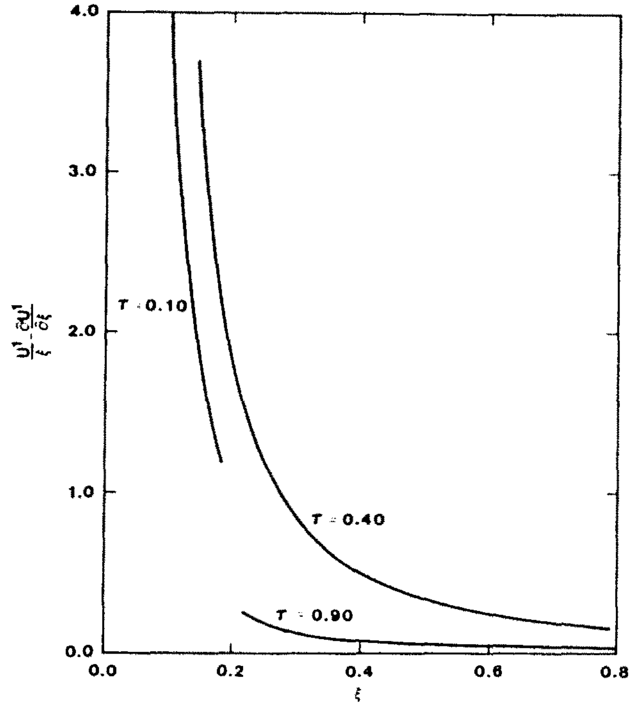

Fig. 6. Criterion of non-negative plastic work for 6.0-*CRH* ogival nose penetrating reinforced concrete ($Y = 95$ MPa) at 1010 m s^{-1}.

Figure 5 shows the radial stresses vs penetration velocity at several locations on a 6.0-*CRH* nose. For a given V, radial stress is a maximum at the tip and decreases as z/l increases. For V approaching zero, all values of S^1 approach the quasi-static solution (23a).

Figure 6 shows three contours at fixed τ of $((U^1/\xi)-(\partial U^1/\partial \xi))$ in the plastic region for a 6.0-*CRH* nose traveling at $V/c_p = 0.5$ ($V = 1010$ m s^{-1}). These contours show that the criterion for non-negative work, inequality (21), is satisfied. These are just a few examples that show this criterion is satisfied, but we made sufficient checks for other parameters, and we feel confident this criterion is satisfied for the applications given in this study.

Figure 7 predicts axial force vs penetration velocity for several nose shapes. As indicated by eqn (1c) and Fig. 1, smaller values of *CRH* represent blunter noses. Forces on all noses approach the quasi-static value for small V, and blunter noses have larger forces as V increases.

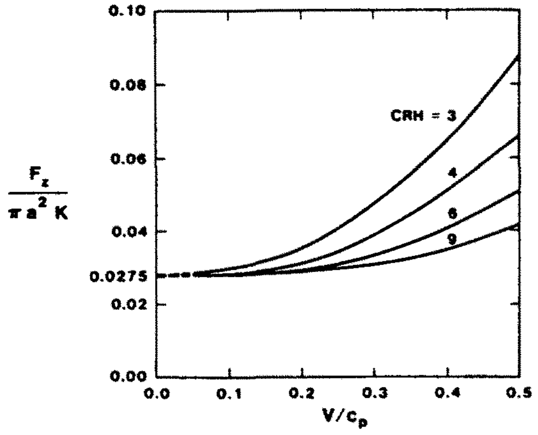

Fig. 7. Axial force on ogival noses vs penetration velocity.

Results in Figs 4–7 are presented for a practical range ($0 < V/c_p < 0.5$). For this concrete, $c_p = 2020$ m s^{-1}, and $0 < V < 1010$ m s^{-1}. As discussed in Ref. [1], field tests with instrumented penetrators can be conducted to $V = 600$ m s^{-1}. In addition, $S^1 = \sigma_r^1/K$ reaches a value of 0.056 at the nosetip for $V = 600$ m s^{-1}. From eqns (3a) and (3b), $p/K = S^1 - T/2$, and the corresponding pressure is 450 MPa. As indicated in Fig. 2, the pressure–volumetric strain data starts to deviate from our linear assumption at about this pressure.

Acknowledgements—The authors thank Dr D. B. Longcope and Mr George Reis of Sandia National Laboratories for many helpful discussions.

REFERENCES

1. M. J. Forrestal, Penetration into dry porous rock. *Int. J. Solids Structures* **22**, 1485–1500 (1986).
2. G. E. Sliter, Assessment of empirical concrete impact formulas. *J. Struct. Div. ASCE* **ST5**, 1023–1045 (May 1970).
3. R. F. Bishop, R. Hill and N. F. Mott, The theory of identation and hardness tests. *Proc. Phys. Soc.* **53**(3), 147–155 (May 1945).
4. R. K. Byers, P. Yarrington and A. J. Chabai, Dynamic penetration of soil media by slender projectiles. *Int. J. Engng Sci.* **16**, 835–844 (1978).
5. M. M. Hightower, The effects of curing and aging on the triaxial properties of concrete in underground structures. *Symposium Proceeding—The Interaction of Non-nuclear Munitions with Structures*, U.S. Air Force Academy, Colorado, pp. 65–68 (May 1983).
6. J. N. Goodier, On the mechanics of indentation and cratering in solid targets of strain-hardening metal by impact of hard and soft spheres. *Proceedings of the 7th Symposium on Hypervelocity Impact*, Vol. III, pp. 215–259. AIAA, New York (1965).
7. S. Hanagud and B. Ross, Large deformation, deep penetration theory for a compressible strain-hardening target material. *AIAA J.* **9**(5), 905–911 (1971).
8. M. J. Forrestal, F. R. Norwood and D. B. Longcope, Penetration into targets described by locked hydrostats and shear strength. *Int. J. Solids Structures* **17**, 915–924 (1981).
9. D. B. Longcope and M. J. Forrestal, Penetration of targets described by a Mohr–Coulomb failure criterion with a tension cutoff. *J. Appl. Mech.* **50**, 327–333 (June 1983).
10. R. Hill, *The Mathematical Theory of Plasticity*. Oxford University Press, London (1950).
11. S. C. Hunter, The propagation of spherically symmetric disturbances in ideally plastic materials. *Proceedings of the Conference on the Properties of Materials at High Rates of Strain*, Institute of Mechanical Engineers, London, pp. 147–155 (April 1957).
12. H. A. Watts, RDEAM—an Adams ODE code with root solving capability, SAND85-1595. Sandia National Laboratories, Albuquerque, New Mexico (October 1985).
13. L. F. Shampine and H. A. Watts, DEPAC—design of a user oriented package of ODE solvers, SAND79-2374. Sandia National Laboratories, Albuquerque, New Mexico (September 1980).